

Grain Boundary Properties of Elemental Metals

Hui Zheng^{a,1}, Xiang-Guo Li^{a,1}, Richard Tran^a, Chi Chen^a, Matthew Horton^b, Donny Winston^b, Kristin Aslaug Persson^{b,c}, Shyue Ping Ong^{a,*}

^a*Department of NanoEngineering, University of California San Diego, 9500 Gilman Dr, Mail Code 0448, La Jolla, CA 92093-0448, United States*

^b*Environmental Energy Technologies Division, Lawrence Berkeley National Laboratory, Berkeley, CA 94720, United States*

^c*Department of Materials Science & Engineering, University of California Berkeley, Berkeley, CA 94720-1760, United States*

Abstract

The structure and energy of grain boundaries (GBs) are essential for predicting the properties of polycrystalline materials. In this work, we use high-throughput density functional theory calculations workflow to construct the Grain Boundary Database (GBDB), the largest database of DFT-computed grain boundary properties to date. The database currently encompasses 327 GBs of 58 elemental metals, including 10 common twist or symmetric tilt GBs for body-centered cubic (bcc) and face-centered cubic (fcc) systems and the $\Sigma 7$ [0001] twist GB for hexagonal close-packed (hcp) systems. In particular, we demonstrate a novel scaled-structural template approach for HT GB calculations, which reduces the computational cost of converging GB structures by a factor of $\sim 3 - 6$. The grain boundary energies and work of separation are rigorously validated against previous experimental and computational data. Using this large GB dataset, we develop an improved predictive model

*Corresponding author

Email address: `ongsp@eng.ucsd.edu` (Shyue Ping Ong)

¹These authors contributed equally

for the GB energy of different elements based on the cohesive energy and shear modulus. The open GBDB represent a significant step forward in the availability of first principles GB properties, which we believe would help guide the future design of polycrystalline materials.

Keywords: Grain boundary, DFT, database, predictive modeling

1. Introduction

The majority of engineering materials are polycrystals, comprising a large number of grains whose interfaces form grain boundaries (GBs). The GB character distribution (GBCD)[1], i.e., the type and frequency of GBs present, strongly affects a material's mechanical properties[2, 3] such as hardness[4], brittleness[5, 6], creep-strength[7], corrosion resistance[8], fatigue strength[9], and weldability[10]. For instance, intergranular fracture is the primary origin of severe brittleness and fatigue failure, and GBs are the preferential sites for the nucleation and propagation of fatigue cracks [5, 11]. Manipulating the GBCD through various processing techniques is a common pathway to improving the mechanical properties of structural metals and alloys. [5, 9, 12, 13, 14].

The GBCD of a material is related to the relative GB formation energies[15]. Typically, the lower the formation energy for a particular type of GB (otherwise simply known as the GB energy or γ_{GB}), the greater its prevalence in the polycrystal[16, 6]. A variety of experimental techniques (e.g., thermal groove, orientation imaging microscopy) have been applied to investigate γ_{GB} , but the data sets were limited due to the difficulty of measuring accurate γ_{GB} [17, 18, 19, 20, 21, 22, 23]. Recently Rohrer et al. have developed a

high-throughput (HT) experimental method to measure γ_{GB} for large ensembles of GBs by inversely correlating it with the statistical abundance of GB types present in the polycrystal [15, 24, 25]. This method has been applied to fcc Ni [26], Ni-based alloys [15], W thin film[27], ferrite (mainly bcc Fe) [28], austenitic steel (mainly fcc Fe)[29] and hcp Ti [30]. Such HT studies have significantly increased the available experimental data for γ_{GB} [16, 26]. However, this statistical approach suffers from a strong dependence of the uncertainty in the measured γ_{GB} on the frequency of observed GBs, leading to unreliable measurements for GBs of lower frequency. Furthermore, the method yields relative, rather than absolute, γ_{GB} .

Computationally, there have been many investigations of γ_{GB} using both empirical and first principles methods. Studies using empirical interatomic potentials (IAPs) such as the embedded atom method (EAM)[31, 32, 33] and Lennard-Jones[31, 32] potentials are typically limited to a few elemental systems belonging to a specific crystal prototype (e.g., fcc or bcc), but cover a broad range of GB types[34, 35, 36, 37, 38, 39]. The reason is because the fitting of sufficiently accurate IAPs is a relatively complex and resource-intensive process, but once fitted, it is inexpensive to use the IAP to compute many GB structures comprising thousands or even millions of atoms. For instance, Olmsted et al. [36], Holm et al. [37, 40] have calculated γ_{GB} for 388 distinct GBs of fcc Ni, Al, Au, and Cu using EAM and found that GB energies in different elements are strongly correlated. For bcc metals, Ratanaphan et al. [39] have computed the energies of 408 distinct GBs in bcc Fe and Mo ranging from $\Sigma 3$ to $\Sigma 323$. Their results show that GB energies are influenced more by GB plane orientation than by lattice misorientation

or lattice coincidence.

With computing advances, calculations of γ_{GB} using accurate, but expensive first-principles methods such as density functional theory (DFT) have become increasingly common. In contrast to IAP-based studies, DFT studies tend to be broader in chemical scope but narrow in the range of GB structures studied (typically limited to low Σ GB models of hundreds of atoms). This is due to the good transferability, but high computational expense, of first principles methods. For example, Scheiber et al. [41] have computed 14 types of GBs for W, Mo and Fe using DFT, while Wang et al. [42] have calculated 11 types of low sigma ($\Sigma < 13$) symmetrical tilt GBs and 2 twist GBs for bcc Fe. Bean and McKenna [43] have also used DFT calculations to verify a small subset of symmetric tilt GB structures acquired from EAM calculations in Cu and Ni systems.

In this work, we report the development of the Grain Boundary DataBase (GBDB), a comprehensive database for GB properties (γ_{GB} , work of separation W_{sep}) for a broad range of low-index GB structures (tilt and twist) for fcc, bcc, and hcp elemental metals using high-throughput DFT calculations. At the time of writing, this GBDB contains data on 327 GB structures for 58 elements, with more GB types and elements continually being added. This GBDB has been made available via the Materials Project and its Application Programming Interface[44, 45], together with a user-friendly web application called Crystal Toolkit for the generation of GB structures. A critical enabler to the construction of the GBDB is an innovative lattice scaling approach, which substantially lowers the computational effort in performing GB calculations for similar crystal types across different elements. Finally,

we rigorously validate the GBDB against prior experimental and computed data, and using this large dataset, develop an efficient model for predicting γ_{GB} for different elements.

2. Methods

2.1. Grain boundary model generation

Figure 1 shows the schematic of the GB model generation algorithm, which is based on the coincident-site lattice (CSL) method [46]. For two grains misoriented by a rotation angle about a rotation axis, the superposition of the two crystals result in coincident sites forming a sublattice of the two crystal lattices, i.e., a CSL. An important parameter characterizing the CSL is the Σ value, defined as the ratio of the unit cell volume of the CSL to the volume of the generating bulk cell. A grain boundary can be completely and unambiguously described by five macroscopic degrees of freedom (DOFs)[47], e.g. $\Sigma 5$ $36.87^\circ/[100](031)$. Three DOFs describe the mutual misorientations between two adjoining grains, two of which define the rotation axis (two DOFs, e.g. $[100]$) and one of which defines the rotation angle, e.g. 36.87° . The remaining two DOFs describe the GB plane, e.g. (031) . The steps in the algorithm are as follows:

- Starting from the unit cell (primitive or conventional cell) with lattice type of cubic, tetragonal, orthorhombic, hexagonal or rhombohedral, a series of lattice vector transformations is performed to create an unit cell of CSL with the a and b lattice vectors parallel to the input GB plane.

- Two grains are created and rotated relative to each other based on the inputs (rotation axis and angle, expansion times of the CSL unit cell along c direction).
- The two grains are then stacked to form the periodic GB structure. The relative shifts between the two grains along the a , b and c directions can be adjusted.
- Finally, sites that are too close to each other based on a distance tolerance set by the user are merged.

The above algorithm is implemented in the open-source Python Materials Genomics (pymatgen) materials analysis library[44], together with methods for finding all sigma values and their corresponding rotation angles for any given input structure and rotation axis. A user-friendly graphical user interface to the algorithm is also available on Materials Project website Crystal Toolkit application (<https://materialsproject.org/#apps/xtaltoolkit>).

2.2. GB property computation

The grain boundary energy (γ_{GB}) is defined by the following expression:

$$\gamma_{GB} = \frac{E_{GB} - n_{GB}E_{bulk}}{2A_{GB}} \quad (1)$$

where E_{GB} and n_{GB} are the total energy and number of atoms of the grain boundary structure, respectively, A_{GB} is the cross-sectional area of the GB, E_{bulk} is the energy per atom of the bulk, and the factor of 2 in the denominator accounts for the two grain boundaries in the GB model.

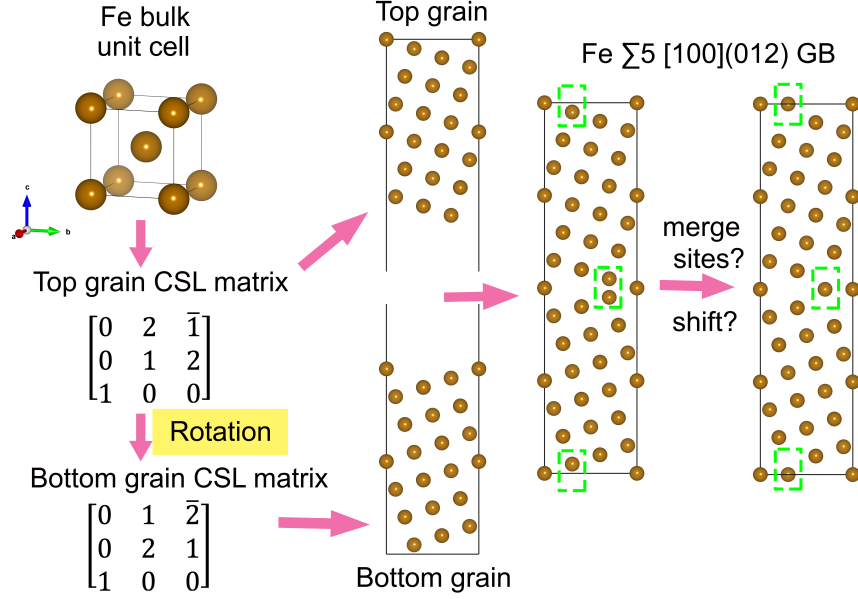


Figure 1: Grain boundary generation process

Another GB property of interest is the work of separation W_{sep} , which is a measure of the energy required to cleave the GB into the free surfaces and is correlated to the fracture toughness[48, 49, 50, 51]. W_{sep} is given by the following expression:

$$W_{sep} = 2\gamma_{surf} - \gamma_{GB} \quad (2)$$

where γ_{surf} is the corresponding surface energy for the facet (hkl) formed by cleaving the GB. Previously, some of the current authors have already constructed a comprehensive database of the surface energies of the elements[52], which are used in this work in the computation of W_{sep} .

2.3. DFT computations

All DFT energy calculations were performed using the Vienna Ab initio Simulation Package (VASP) [53] with the projector augmented wave

(PAW) [54, 55] method. The exchange-correlation effects were modeled using the Perdew-Berke-Ernzerhof (PBE) [56] generalized gradient approximation (GGA) functional. The plane wave energy cutoff is 400 eV, and k -point grids of 30 \AA^{-1} and 45 \AA^{-1} in each lattice direction were used for relaxation and single-point energy calculations, respectively. The energies and atomic forces of all calculations were converged within 10^{-4} eV and 0.02 eV \AA^{-1} . Through a series of convergence tests, it was determined that a thickness of at least 25 \AA along the direction normal to the GB plane is sufficient to minimize periodic interactions between the two grain boundaries, such that γ_{GB} is converged to within 0.02 J m^{-2} .

2.4. Scope of Data

Our database covers a total of 58 elements (see Figure 2), with 10 GB types for fcc and bcc and one GB type for hcp and double-hcp (dhcp) elements (see Table 1), with a total of 327 GB structures. We limit the GB types in this study with the following criteria:

1. $\Sigma < 10$
2. Maximum Miller index (MMI) of rotation axis ≤ 1
3. MMI of grain boundary plane ≤ 3 .
4. All tilt GBs are symmetric.

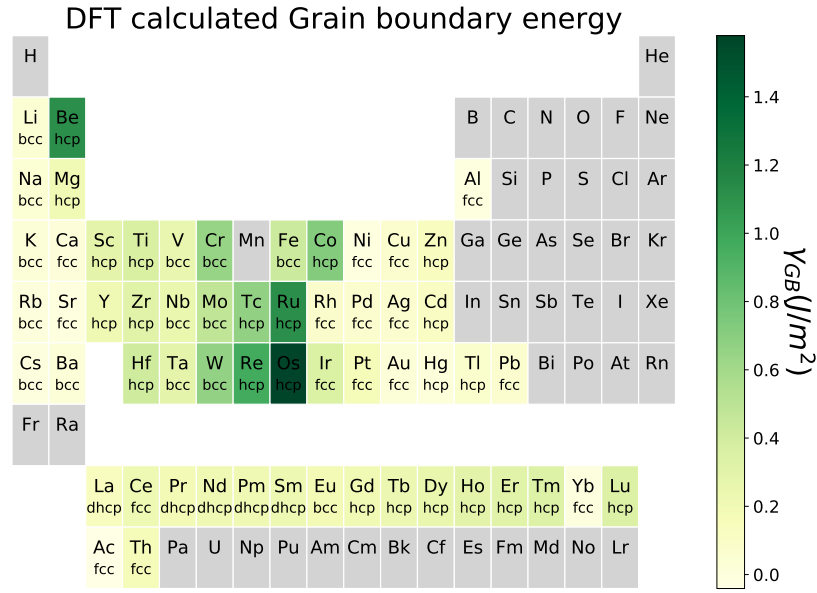


Figure 2: DFT calculated grain boundary energy. For bcc and fcc, the lowest γ_{GB} types, i.e., $\Sigma 3[110](112)$ for bcc and $\Sigma 3111$ for fcc are plotted. For hcp, and double-hcp (dhcp) elements, $\Sigma 7(0001)$ GBs are chosen to be represented in this periodic table heatmap.

Sigma	type	R-axis	R-angle	GB-plane	Join-plane	bcc atoms	fcc atoms
bcc or fcc							
3	tilt	[110]	109.47	$(1 \bar{1} \bar{2})$	$(\bar{1} 1 \bar{2})$	24	46
3	tilt	[111]	180	$(1 \bar{1} 0)$	$(0 1 \bar{1})$	48	56
3	twist	[111]	60	$(1 1 1)$	$(1 1 1)$	48	24
5	tilt	[100]	36.87	$(0 \bar{1} \bar{2})$	$(0 2 1)$	38	38
5	tilt	[100]	53.13	$(0 \bar{1} \bar{3})$	$(0 3 1)$	40	58
5	twist	[100]	36.87	$(1 0 0)$	$(1 0 0)$	80	80
7	twist	[111]	38.21	$(1 1 1)$	$(1 1 1)$	168	84
7	tilt	[111]	38.21	$(1 \bar{3} 2)$	$(\bar{2} 3 \bar{1})$	54	54
9	twist	[110]	38.94	$(1 1 0)$	$(1 1 0)$	126	180
9	tilt	[110]	38.94	$(2 \bar{2} \bar{1})$	$(2 \bar{2} 1)$	70	70
hcp/dhcp						hcp/dhcp atoms	
7	twist	[0001]	21.79	$(0 0 0 1)$	$(0 0 0 1)$	112	

Table 1: Grain boundary types calculated in this work

3. Results

3.1. Benchmarking

A major bottleneck to calculations of GBs is that the large system sizes combined with difficult convergence of atomic positions, especially close to the GB region, render such computations relatively expensive compared to bulk crystal calculations. To accelerate such computations, a fundamental hypothesis explored in this work is that similar crystal structures (e.g., bcc, fcc, or hcp) lead to similar low-energy GB configurations.

To find the most favorable initial configurations of GBs, we applied rigid body translation [38] of two grains to each type of twist GBs by performing a series of static calculations for each translation vector. The translation unit step length along the \mathbf{c} direction is in increments of 10% of the lattice parameter of the conventional unit cell. While along the basal directions (\mathbf{a} and \mathbf{b}), the translation unit step is in increments of 5% - 10% of the basal lattice vectors (\mathbf{a} and \mathbf{b}) of the GB structure. For symmetric tilt GBs, atoms at the interface that are less than 70% of the bulk interatomic distance apart are merged. We find that the most favorable initial configurations are identical for crystals of the same prototype (see Figure S1 and S2).

Based on these results, we have developed a high-throughput workflow for GB calculations using the Atomate software package [44, 57, 58], as shown in Figure 3. For each structural prototype (bcc, fcc, hcp and dhcp), we first compute a series of fully-relaxed GB templates for all the GB types investigated in this work (see Table 1), using Mo, Cu and Be/La as the templates for bcc, fcc and hcp/dhcp structures, respectively. Initial structures for GB computations of each element M are then created from these GB templates by applying a scaling factor of $\frac{a_M}{a_{prototype}}$ to the template GB lattice constants for all materials, where a_M and $a_{prototype}$ are the bulk lattice parameters of the metal M and prototype element respectively. No scaling is applied for Zn and Cd, which are hcp elements with c/a ratios (1.986 and 1.915, respectively) that deviate substantially from the ideal ratio of 1.633, and their GB structures were generated directly from the bulk structure. A full relaxation is then performed on the scaled GBs. The use of the scaled GB templates significantly reduces the computational resources for the most time-consuming

structural relaxation step by a factor of $\sim 3 - 6$, with higher speed-ups for GBs with larger number of atoms and GBs that are very different from bulk (Table 2). More accurate static calculations with denser k -point meshes were then performed to obtain the final total energy of the GB structures. The results were then automatically inserted into a MongoDB document-based database.

Element	GB type	# of atoms	CPU hours		Speed up
			No template	With template	
bcc-Ba	$\Sigma 3(111)$	48	2560.00	716.80	3.57
bcc-Fe	$\Sigma 9(110)$	126	2340.00	508.33	4.60
fcc-Sr	$\Sigma 5(100)$	80	2128.05	344.29	6.18
fcc-Ag	$\Sigma 5(013)$	80	97.67	97.55	1.00
hcp-Ti	$\Sigma 7(0001)$	112	24.28	13.94	1.74
dhcp-Nd	$\Sigma 7(0001)$	112	218.39	59.08	3.70

Table 2: CPU hours for GB relaxation with and without the use of scaled prototype templates.

3.2. Grain boundary energies

Figure 4 shows the distribution of γ_{GB} for bcc, fcc, and hcp elements. All values are tabulated in Table S1 and S2 for reference. For bcc elements (Figure 4a), we can observe a substantial jump in γ_{GB} from alkali/alkaline earth metals to transition metals; the γ_{GB} for alkali and alkaline earth metals are less than 0.3 Jm^{-2} , while those for the transition metals are at least four times higher. γ_{GB} for fcc elements follows a similar trend but with a more

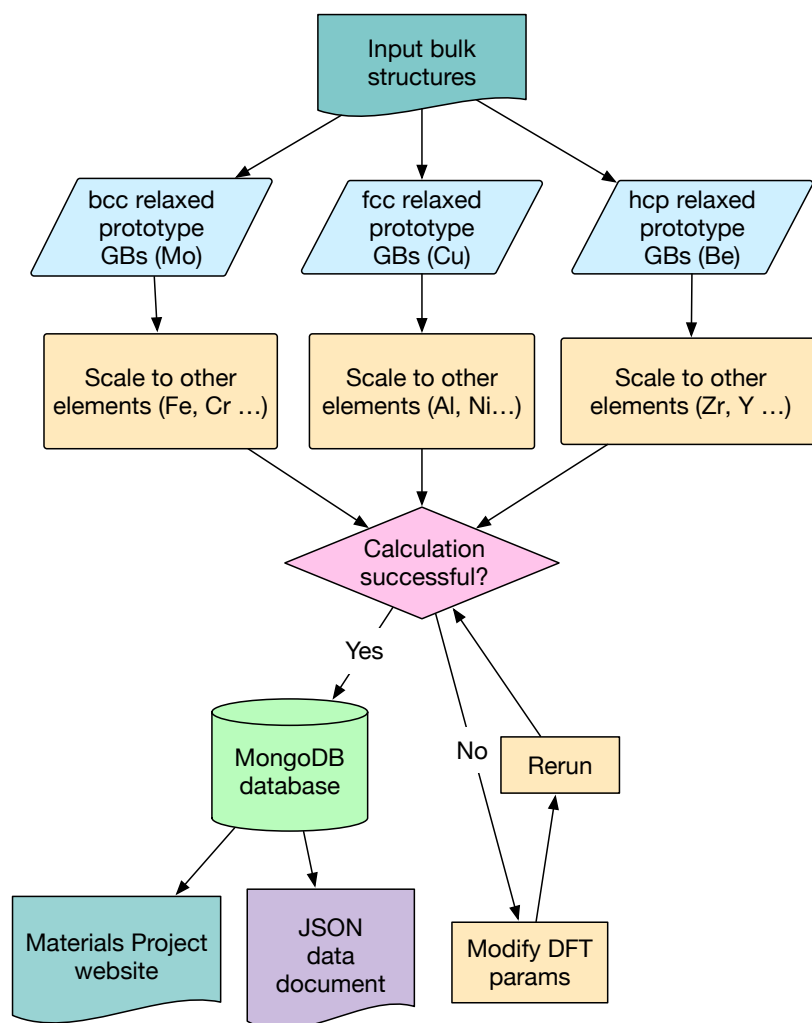


Figure 3: High-throughput computational workflow for elemental grain boundaries.

gradual increase (see Figure 4b). Group VIII elements have high γ_{GB} while group IB, IIA, and IIB elements have relatively low γ_{GB} .

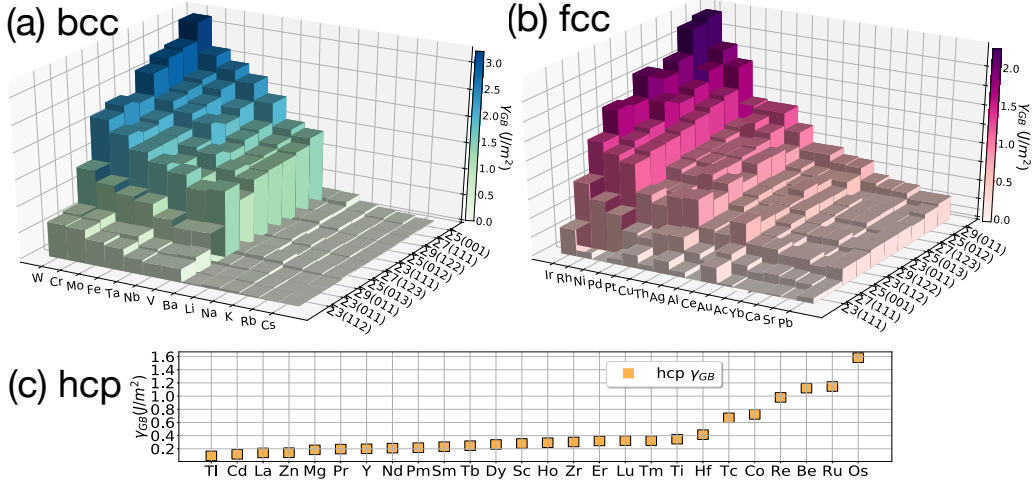


Figure 4: Grain boundary energy γ_{GB} distribution for (a) bcc, (b) fcc, and (c) hcp/dhcp elemental metals, sorted by increasing γ_{GB} .

Figure 4c shows the γ_{GB} distribution for hcp/dhcp $\Sigma 7(0001)$ grain boundaries. For transition metals, we observe that γ_{GB} peaks at groups VIIB and VIII (Tc, Co, Re, Ru, and Os). All the rare earth and group IIA elements have lower GB energies than the transition metals with the exception of Be, which has a much higher GB energy. The rare earth elements show a gradual increase in γ_{GB} as group number increases.

The γ_{GB} distribution across different GB types varies with the crystal type. The two coherent twin boundaries, $\Sigma 3(111)$ for fcc and $\Sigma 3(112)$ for bcc, have the lowest γ_{GB} within the respective crystal prototypes. GBs terminated by the most atomically-dense planes ((111) for fcc and (110) for bcc) have lower γ_{GB} than other planes in general. Consequently, the fcc $\Sigma 7(111)$ and bcc $\Sigma 3(011)$ GBs correspond to the second lowest γ_{GB} for

fcc and bcc, respectively. This is in agreement with both previous atomistic calculations[37, 39, 59, 32, 33] and experimental results[16, 40, 60, 27]. For example, it has been observed experimentally that the most frequently observed grain boundary for fcc Ni and Al is the $\Sigma 3(111)$ twin boundary, and other GBs terminated with the (111) plane also have a high population[26, 60]. For bcc metals, our data shows that the $\Sigma 3(112)$ symmetric tilt GB (twin) has the lowest energy, which agrees with experiments performed in bcc W thin films[27] with nanoscale grain sizes and bcc ferritic/interstitial free steel[28, 61].

Figure 5 shows the validation of our computed γ_{GB} with previous DFT calculations [41, 42, 62, 63, 64, 65, 66, 67, 43, 68] , atomistic calculations[69] using machine-learned spectral neighbor analysis potentials (SNAP)[70, 71] and the embedded atom method (EAM)[39, 36, 40], and experimental data[26, 16, 61, 27]. From Figure 5a and Table S5 we may observe that our computed γ_{GB} are in excellent agreement with previous DFT values, with a R^2 close to unity and a very small standard error of 0.013 J/m². Similarly, we find good agreement between the calculated γ_{GB} for different GBs of Mo and Ni with those computed using the state-of-the-art SNAP models[70, 71], while the EAM predicted GB energies[36, 39] are substantially underestimated as shown in Figure 5(b) and (c). For bcc Mo, values of γ_{GB} using SNAP are slightly larger than most DFT values with the exception of the $\Sigma 5(012)$ GB where SNAP slightly underestimates DFT values. For fcc Ni, the γ_{GB} values of both EAM and SNAP are consistent with our DFT values, further supporting the conclusion that EAM performs better in fcc systems than bcc systems[71].

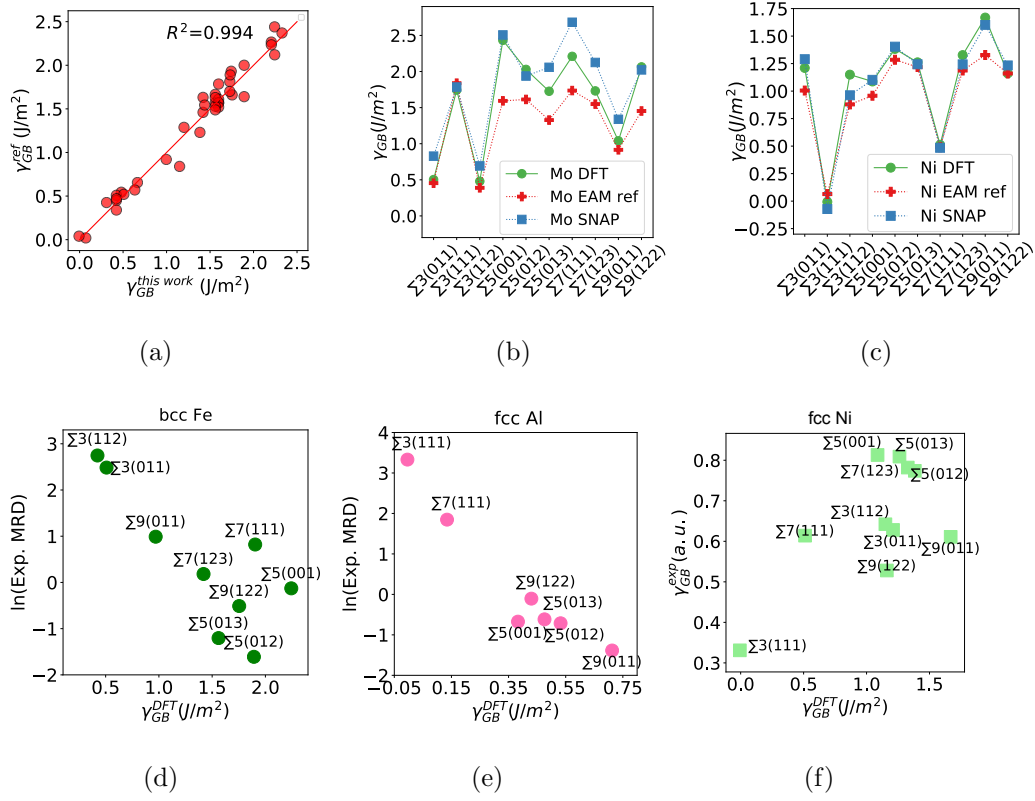


Figure 5: Comparison of γ_{GB} between this work and (a) previous DFT values; (b, c) EAM [36, 39] and SNAP[70, 71] values. (d), (e) and (f) compare our the calculated γ_{GB} of bcc Fe, fcc Al, and fcc Ni with experimentally measured MRD[61, 60] and γ_{GB} [26].

Figures 5(d) and (e) plot the natural log of the experimentally measured multiples of random distribution (MRD), i.e. the experimental average population of GBs, against the DFT calculated grain boundary energy (γ_{GB}^{DFT}) for Fe and Al, respectively. We observe a negative correlation between the $\ln(MRD)$ and γ_{GB} similar to that reported previously for Ni[26]. Figure 5 (f) plots the experimental grain boundary energy (γ_{GB}^{exp})[26] against our γ_{GB}^{DFT} values for Ni. All values of γ_{GB}^{exp} are derived from a statistical average

of the MRD and given in arbitrary units. We also observe a general positive correlation between γ_{GB}^{exp} and γ_{GB}^{DFT} .

3.3. Work of separation

The thermodynamic threshold energy for GB fracture, or work of separation (W_{sep}), can be defined as the difference between the surface energy and GB energy as shown in equation (2). Since the formation of surfaces and GBs both relate to bond breaking and distortion, we expect grain boundary energy γ_{GB} , surface energy γ_{surf} and work of separation W_{sep} to be positively correlated with cohesive energy. This is demonstrated in Figure 6 for bcc $\Sigma 3(110)$, fcc $\Sigma 3(111)$ and hcp $\Sigma 7(0001)$ GBs. The values of W_{sep} for all other GB types are provided in Table S3 and S4. This positive correlation is in agreement with previous bond breaking arguments [34, 35]. In general, the variation in anisotropic surface energies across different surfaces is smaller compared to the GB energy variation across different types of GBs as shown in Figure S3. As such, we can expect a negative correlation between GB energy and work of separation as shown in Figure S4.

Figure 7 plots the experimentally measured ultimate tensile strength (UTS)[72] against the calculated W_{sep} for the GB with lowest γ_{GB} , i.e., the likely dominant GB type. A general positive relationship is observed between W_{sep} and UTS, as expected. The non-monotonic relationship may be due to the different processing methods (e.g., annealing, heat treatment, cold-worked) that can significantly affect micro-structure, and hence measured UTS.

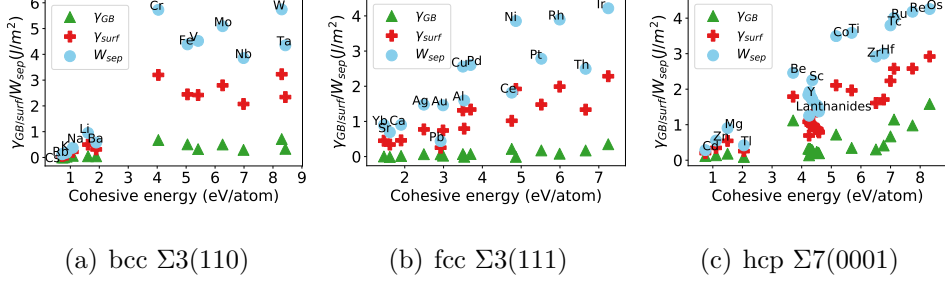


Figure 6: Comparison between surface energy (γ_{surf}), grain boundary energy (γ_{GB}) and work of separation (W_{sep}) for (a) bcc $\Sigma 3(110)$, (b) fcc $\Sigma 3(111)$ and (c) hcp $\Sigma 7(0001)$ GBs, plotted in order of ascending cohesive energy E_{coh} of the element.

3.4. Multiple linear regression model for γ_{GB}

Using the extensive set of computed γ_{GB} , we have developed a multiple linear regression (MLR) model for γ_{GB} for each GB type by fitting to the following equation:

$$\widehat{\gamma_{GB}} = \beta_1 E_{coh} a_0^{-2} + \beta_2 G \cdot a_0 \quad (3)$$

where $\widehat{\gamma_{GB}}$ is the fitted grain boundary energy, E_{coh} is the cohesive energy, a_0 is the lattice parameter of corresponding conventional bulk cell (Å), and G is the shear modulus (Jm^{-3})[73]. This model choice is an amalgamation of models proposed in previous works. Ratanaphan et al. have found that the γ_{GB} of bcc Fe and Mo are strongly correlated with the cohesive energy (E_{coh})[39]. Previous EAM-based GB databases have also found that γ_{GB} for fcc metals such as Al, Au, Cu and Ni are strongly correlated to the Voigt average shear modulus (C_{44})[37, 36]. Furthermore, the Read-Shockley dislocation model[74] treats GBs with small misorientation angles as an array of dislocations whose energy is proportional to a shear modulus. In essence, the

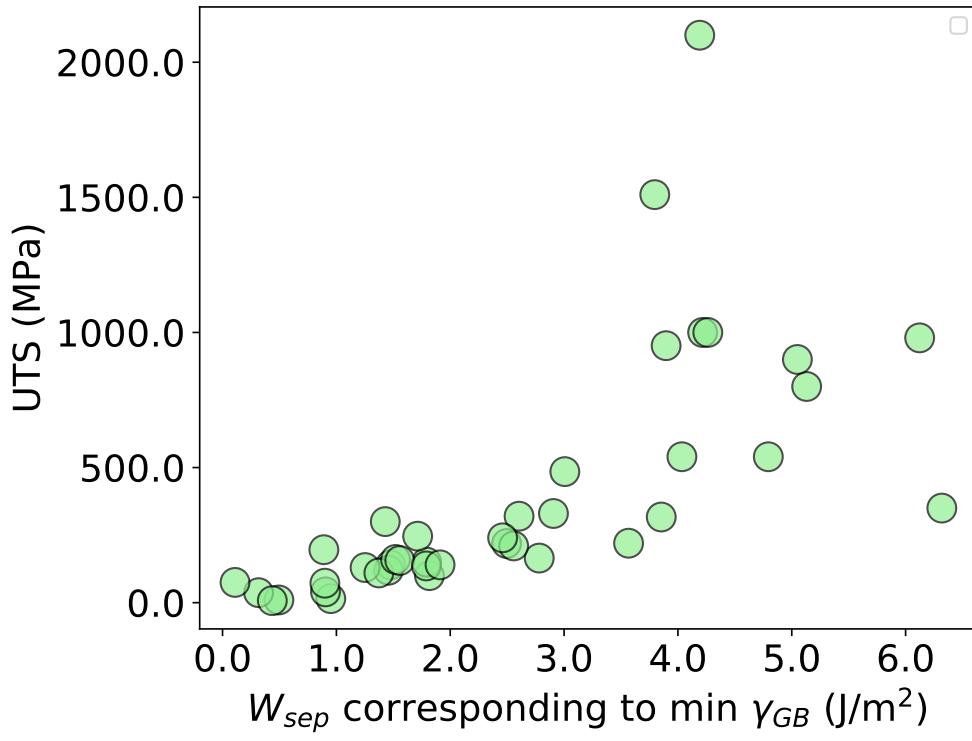


Figure 7: Relationship between calculated work of separation W_{sep} for GB with lowest γ_{GB} and experimentally measured ultimate tensile strength (UTS) [72].

$E_{coh}a_0^{-2}$ term in equation (3) accounts for the contribution of broken bonds to γ_{GB} , while the $G \cdot a_0$ term accounts for the contributions from distorted (stretched, compressed) bonds. Both terms have been scaled by powers of the lattice constant such that the coefficients β_1 and β_2 are dimensionless.

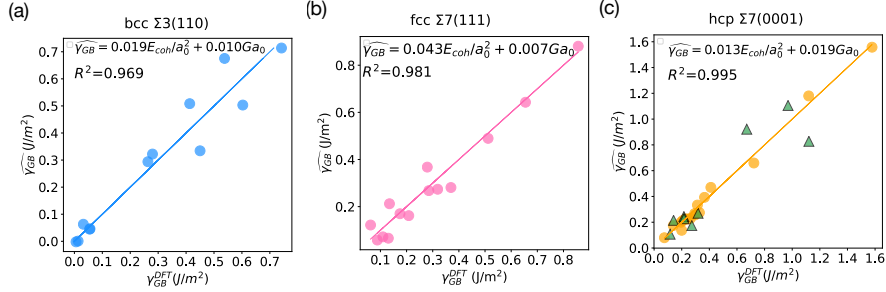


Figure 8: Multiple linear regression models for the (a) bcc $\Sigma 3(110)$, (b) fcc $\Sigma 7(111)$, and (c) hcp $\Sigma 7(0001)$ GBs.

Figure 8 shows the fitting results for three GB types (see Figure S5 and S6 for the remaining GB types). In general, the MLR models exhibit good predictive accuracy across all GB types, with $R^2 > 0.9$. We note that each GB type has different fitted values of the dimensionless coefficients β_1 and β_2 due to different contributions from bond breaking and bond distortion. We provide an example to show the predictive ability of our linear regression model. In Figure 8(c), the orange circles are the data points used to build the MLR model, and the green triangles are a “test set” of elemental GBs. It can be seen that the performance on the “test set” is similar to that of the training set. We show that these results hold for all the GB structures computed in this work, and we believe it will hold for GB structures of larger Σ values for which the model GB structure can contain many more atoms and hence are more expensive to compute. The implication of these results is

that a predictive MLR model can potentially be constructed using a smaller set of elements with a range of E_{coh} and G , and use to extrapolate to other elements.

4. Conclusion

The GBDB is, to the best of our knowledge, the most comprehensive database of DFT computed GB energies and work of separation to date, spanning 10 different of GB types, including both tilt and twist GBs, across 58 types of metals. This GBDB has been rigorously validated with previous computational values as well as experimental observations of the GBCD[60, 15, 16, 24, 27, 61, 39]. The linear regression model provides an inexpensive estimate for the GB energy of elemental metals using cohesive energy and shear modulus.

5. Acknowledgement

This work is supported by the Materials Project, funded by the U.S. Department of Energy, Office of Science, Office of Basic Energy Sciences, Materials Sciences and Engineering Division under Contract no. DE-AC02-05-CH11231: Materials Project program KC23MP. The authors also acknowledge computational resources provided by the National Energy Research Scientific Computing Centre (NERSC), the Triton Shared Computing Cluster (TSCC) at the University of California, San Diego, and the Extreme Science and Engineering Discovery Environment (XSEDE) supported by National Science Foundation under grant no. ACI-1053575. The authors thank Professor Gregory S. Rohrer from Carnegie Mellon University for providing the

exact values of the experimental grain boundary energies of Ni from ref [26].

6. References

References

- [1] T. Watanabe, The importance of grain boundary character distribution (GBCD) to recrystallization, grain growth and texture, *Scripta Metallurgica et Materialia* 27 (1992) 1497–1502.
- [2] G. S. Rohrer, Grain boundary energy anisotropy: a review, *Journal of Materials Science* 46 (2011) 5881–5895.
- [3] T. Watanabe, Grain boundary engineering: Historical perspective and future prospects, *Journal of Materials Science* 46 (2011) 4095–4115.
- [4] C. Hu, J. Huang, B. G. Sumpter, E. Meletis, T. Dumitric, Ab Initio Predictions of Strong Interfaces in Transition-Metal Carbides and Nitrides for Superhard Nanocomposite Coating Applications, *ACS Applied Nano Materials* 1 (2018) 2029–2035.
- [5] T. Watanabe, S. Tsurekawa, The control of brittleness and development of desirable mechanical properties in polycrystalline systems by grain boundary engineering, *Acta Materialia* 47 (1999) 4171–4185.
- [6] H. Zheng, R. Tran, X. G. Li, B. Radhakrishnan, S. P. Ong, Role of Zr in strengthening MoSi₂ from density functional theory calculations, *Acta Materialia* 145 (2018) 470–476.

- [7] E. M. Lehigh, G. Palumbo, On the creep behaviour of grain boundary engineered nickel 1, *Materials Science and Engineering: A* 237 (1997) 168–172.
- [8] P. Shi, R. Hu, T. Zhang, L. Yuan, J. Li, Grain boundary character distribution and its effect on corrosion of Ni23Cr16Mo superalloy, *Materials Science and Technology* 33 (2017) 84–91.
- [9] S. Kobayashi, T. Inomata, H. Kobayashi, S. Tsunekawa, T. Watanabe, Effects of grain boundary- and triple junction-character on intergranular fatigue crack nucleation in polycrystalline aluminum, *Journal of Materials Science* 43 (2008) 3792–3799.
- [10] E. M. Lehigh, G. Palumbo, P. Lin, Improving the weldability and service performance of nickel-and iron-based superalloys by grain boundary engineering, *Metallurgical and Materials Transactions A* 29 (1998) 3069–3079.
- [11] G. S. Was, Grain-Boundary Chemistry and Intergranular Fracture in Austenitic Nickel-Base Alloys A Review, *CORROSION* 46 (1990) 319–330.
- [12] T. Watanabe, Grain boundary engineering: historical perspective and future prospects, *Journal of Materials Science* 46 (2011) 4095–4115.
- [13] U. Krupp, W. M. Kane, X. Liu, O. Dueber, C. Laird, C. J. McMahon, The effect of grain-boundary-engineering-type processing on oxygen-induced cracking of IN718, *Materials Science and Engineering: A* 349 (2003) 213–217.

- [14] A. Pineau, Crossing grain boundaries in metals by slip bands, cleavage and fatigue cracks, *Philosophical Transactions of the Royal Society A: Mathematical, Physical and Engineering Sciences* 373 (2015) 20140131.
- [15] G. S. Rohrer, J. Li, S. Lee, A. D. Rollett, M. Groeber, M. D. Uchic, Deriving grain boundary character distributions and relative grain boundary energies from three-dimensional EBSD data, *Materials Science and Technology* 26 (2010) 661–669.
- [16] G. S. Rohrer, E. A. Holm, A. D. Rollett, S. M. Foiles, J. Li, D. L. Olmsted, Comparing calculated and measured grain boundary energies in nickel, *Acta Materialia* 58 (2010) 5063–5069.
- [17] G. Hasson, J.-Y. Boos, I. Herbeuval, M. Biscondi, C. Goux, Theoretical and experimental determinations of grain boundary structures and energies: Correlation with various experimental results, *Surface Science* 31 (1972) 115–137.
- [18] K. Barmak, J. Kim, C.-S. Kim, W. E. Archibald, G. S. Rohrer, A. D. Rollett, D. Kinderlehrer, S. Ta’asan, H. Zhang, D. J. Srolovitz, Grain boundary energy and grain growth in Al films: Comparison of experiments and simulations, *Scripta Materialia* 54 (2006) 1059–1063.
- [19] N. A. Gjostein, F. N. Rhines, Absolute interfacial energies of [001] tilt and twist grain boundaries in copper, *Acta Metallurgica* 7 (1959) 319–330.
- [20] M. McLean, Grain-boundary energy of copper at 1030C, *Journal of Materials Science* 8 (1973) 571–576.

- [21] S. W. Chan, R. W. Balluffi, Study of energy vs misorientation for grain boundaries in gold by crystallite rotation method-II. Tilt boundaries and mixed boundaries, *Acta Metallurgica* 34 (1986) 2191–2199.
- [22] H. Miura, M. Kato, T. Mori, Temperature dependence of the energy of Cu [110] symmetrical tilt grain boundaries, *Journal of Materials Science Letters* 13 (1994) 46–48.
- [23] T. Skidmore, R. G. Buchheit, M. C. Juhas, Grain boundary energy vs. misorientation in Inconel® 600 alloy as measured by thermal groove and OIM analysis correlation, *Scripta Materialia* 50 (2004) 873–877.
- [24] G. S. Rohrer, Measuring and interpreting the structure of grain-boundary networks, *Journal of the American Ceramic Society* 94 (2011) 633–646.
- [25] Y. Amouyal, E. Rabkin, Y. Mishin, Correlation between grain boundary energy and geometry in Ni-rich NiAl, *Acta Materialia* 53 (2005) 3795–3805.
- [26] J. Li, S. J. Dillon, G. S. Rohrer, Relative grain boundary area and energy distributions in nickel, *Acta Materialia* 57 (2009) 4304–4311.
- [27] X. Liu, D. Choi, H. Beladi, N. T. Nuhfer, G. S. Rohrer, K. Barmak, The five-parameter grain boundary character distribution of nanocrystalline tungsten, *Scripta Materialia* 69 (2013) 413–416.
- [28] H. Beladi, G. S. Rohrer, The relative grain boundary area and energy distributions in a ferritic steel determined from three-dimensional electron backscatter diffraction maps, *Acta Materialia* 61 (2013) 1404–1412.

- [29] H. Beladi, N. T. Nuhfer, G. S. Rohrer, The five-parameter grain boundary character and energy distributions of a fully austenitic high-manganese steel using three dimensional data, *Acta Materialia* 70 (2014) 281–289.
- [30] M. N. Kelly, K. Glowinski, N. T. Nuhfer, G. S. Rohrer, The five parameter grain boundary character distribution of α -Ti determined from three-dimensional orientation data, *Acta Materialia* 111 (2016) 22–30.
- [31] D. Wolf, Structure-energy correlation for grain boundaries in F.C.C. metalsI. Boundaries on the (111) and (100) planes, *Acta Metallurgica* 37 (1989) 1983–1993.
- [32] D. Wolf, S. Phillpot, Role of the densest lattice planes in the stability of crystalline interfaces: A computer simulation study, *Materials Science and Engineering: A* A107 (1989) 3–14.
- [33] D. Wolf, Correlation between the energy and structure of grain boundaries in b.c.c. metals. II. Symmetrical tilt boundaries, *Philosophical Magazine A* 62 (1990) 447–464.
- [34] D. Wolf, A broken-bond model for grain boundaries in face-centered cubic metals, *Journal of Applied Physics* 68 (1990) 3221–3236.
- [35] D. Wolf, Structure-energy correlation for grain boundaries in F.C.C. metals-III. Symmetrical tilt boundaries, *Acta Metallurgica Et Materialia* 38 (1990) 781–790.
- [36] D. L. Olmsted, S. M. Foiles, E. A. Holm, Survey of computed grain

- boundary properties in face-centered cubic metals: I. Grain boundary energy, *Acta Materialia* 57 (2009) 3694–3703.
- [37] E. A. Holm, D. L. Olmsted, S. M. Foiles, Comparing grain boundary energies in face-centered cubic metals: Al, Au, Cu and Ni, *Scripta Materialia* 63 (2010) 905–908.
 - [38] M. A. Tschopp, S. P. Coleman, D. L. McDowell, Symmetric and asymmetric tilt grain boundary structure and energy in Cu and Al (and transferability to other fcc metals), *Integrating Materials and Manufacturing Innovation* 4 (2015) 11.
 - [39] S. Ratanaphan, D. L. Olmsted, V. V. Bulatov, E. A. Holm, A. D. Rollett, G. S. Rohrer, Grain boundary energies in body-centered cubic metals, *Acta Materialia* 88 (2015) 346–354.
 - [40] E. A. Holm, G. S. Rohrer, S. M. Foiles, A. D. Rollett, H. M. Miller, D. L. Olmsted, Validating computed grain boundary energies in fcc metals using the grain boundary character distribution, *Acta Materialia* 59 (2011) 5250–5256.
 - [41] D. Scheiber, R. Pippan, P. Puschnig, L. Romaner, Ab initio calculations of grain boundaries in bcc metals, *Modelling and Simulation in Materials Science and Engineering* 24 (2016) 035013.
 - [42] J. Wang, G. K. H. Madsen, R. Drautz, Grain boundaries in bcc-fe: a density-functional theory and tight-binding study, *Modelling and Simulation in Materials Science and Engineering* 26 (2018) 025008.

- [43] J. J. Bean, K. P. McKenna, Origin of differences in the excess volume of copper and nickel grain boundaries, *Acta Materialia* 110 (2016) 246–257.
- [44] S. P. Ong, W. D. Richards, A. Jain, G. Hautier, M. Kocher, S. Cholia, D. Gunter, V. L. Chevrier, K. A. Persson, G. Ceder, Python Materials Genomics (pymatgen): A robust, open-source python library for materials analysis, *Computational Materials Science* 68 (2013) 314–319.
- [45] S. P. Ong, S. Cholia, A. Jain, M. Brafman, D. Gunter, G. Ceder, K. A. Persson, The Materials Application Programming Interface (API): A simple, flexible and efficient API for materials data based on REpresentational State Transfer (REST) principles, *Computational Materials Science* 97 (2015) 209–215.
- [46] H. Grimmer, Coincidence-site lattices, *Acta Crystallographica Section A* 32 (1976) 783–785.
- [47] P. Lejček, Grain Boundaries: Description, Structure and Thermodynamics, in: *Grain boundary Segregation in Metals*, 2010, pp. 5–24.
- [48] J. J. Möller, E. Bitzek, Fracture toughness and bond trapping of grain boundary cracks, *Acta Materialia* 73 (2014) 1–11.
- [49] V. R. Coffman, J. P. Sethna, Grain boundary energies and cohesive strength as a function of geometry, *Physical Review B* 77 (2008) 144111.
- [50] M. Grujicic, H. Zhao, G. L. Krasko, Atomistic simulation of 3 (111) grain boundary fracture in tungsten containing various impurities, *International Journal of Refractory Metals and Hard Materials* 15 (1997) 341–355.

- [51] P. Gumbsch, Atomistic modelling of diffusion-controlled interfacial decohesion, *Materials Science and Engineering: A* 260 (1999) 72–79.
- [52] R. Tran, Z. Xu, B. Radhakrishnan, D. Winston, W. Sun, K. A. Persson, S. P. Ong, Data Descriptor: Surface energies of elemental crystals, *Scientific Data* 3 (2016) 1–13.
- [53] W. Kohn, L. J. Sham, Self-consistent equations including exchange and correlation effects, *Phys. Rev.* 140 (1965) A1133–A1138.
- [54] G. Kresse, J. Furthmüller, Efficient iterative schemes for ab initio total-energy calculations using a plane-wave basis set, *Physical Review B* 54 (1996) 11169–11186.
- [55] P. E. Blöchl, Projector augmented-wave method, *Physical Review B* 50 (1994) 17953–17979.
- [56] J. P. Perdew, K. Burke, M. Ernzerhof, Generalized Gradient Approximation Made Simple, *Physical Review Letters* 77 (1996) 3865–3868.
- [57] K. Mathew, J. H. Montoya, A. Faghaninia, S. Dwarakanath, M. Aykol, H. Tang, I.-h. Chu, T. Smidt, B. Bocklund, M. Horton, J. Dagdelen, B. Wood, Z.-k. Liu, J. Neaton, S. Ping, K. Persson, A. Jain, S. P. Ong, K. Persson, A. Jain, S. Ping, K. Persson, A. Jain, Atomate: A high-level interface to generate, execute, and analyze computational materials science workflows, *Computational Materials Science* 139 (2017) 140–152.
- [58] A. Jain, S. P. Ong, W. Chen, B. Medasani, X. Qu, M. Kocher, M. Brafman, G. Petretto, G.-M. Rignanese, G. Hautier, D. Gunter, K. A.

- Persson, FireWorks: a dynamic workflow system designed for high-throughput applications, *Concurrency and Computation: Practice and Experience* 27 (2015) 5037–5059.
- [59] D. Wolf, Structure and energy of general grain boundaries in bcc metals, *Journal of Applied Physics* 69 (1991) 185–196.
 - [60] D. M. Saylor, B. S. El Dasher, A. D. Rollett, G. S. Rohrer, Distribution of grain boundaries in aluminum as a function of five macroscopic parameters, *Acta Materialia* 52 (2004) 3649–3655.
 - [61] H. Beladi, G. S. Rohrer, The distribution of grain boundary planes in interstitial free steel, *Metallurgical and Materials Transactions A: Physical Metallurgy and Materials Science* 44 (2013) 115–124.
 - [62] S. K. Bhattacharya, S. Tanaka, Y. Shihara, M. Kohyama, Ab initio study of symmetrical tilt grain boundaries in bcc Fe: structural units, magnetic moments, interfacial bonding, local energy and local stress, *Journal of Physics: Condensed Matter* 25 (2013) 135004.
 - [63] E. Wachowicz, T. Ossowski, A. Kiejna, Cohesive and magnetic properties of grain boundaries in bcc Fe with Cr additions, *Phys. Rev. B* 81 (2010) 94104.
 - [64] N. Gao, C. C. Fu, M. Samaras, R. Schaublin, M. Victoria, W. Hoffelner, Multiscale modelling of bi-crystal grain boundaries in bcc iron, *Journal of Nuclear Materials* 385 (2009) 262–267.
 - [65] Y. A. Du, L. Ismer, R. Jutta, T. Hickel, J. Neugebauer, R. Drautz,

- First-principles study on the interaction of H interstitials with grain boundaries in α and γ -Fe, *Phys. Rev. B* 84 (2011) 144121.
- [66] M. Čák, M. Šob, J. Hafner, First-principles study of magnetism at grain boundaries in iron and nickel, *Physical Review B - Condensed Matter and Materials Physics* 78 (2008) 1–10.
 - [67] T. Ochs, C. Elsässer, M. Mrovec, V. Vitek, J. Belak, J. A. Moriarty, Symmetrical tilt grain boundaries in bcc transition metals: Comparison of semiempirical with ab-initio total-energy calculations, *Philosophical Magazine A: Physics of Condensed Matter, Structure, Defects and Mechanical Properties* 80 (2000) 2405–2423.
 - [68] A. F. Wright, S. R. Atlas, Density-functional calculations for grain boundaries in aluminum, *Phys. Rev. B* 50 (1994) 15248–15260.
 - [69] S. Plimpton, Fast Parallel Algorithms for Short-Range Molecular Dynamics, *Journal of Computational Physics* 117 (1995) 1–19.
 - [70] C. Chen, Z. Deng, R. Tran, H. Tang, I.-h. Chu, S. P. Ong, Accurate force field for molybdenum by machine learning large materials data, *Physical Review Materials* 1 (2017) 043603.
 - [71] X.-G. Li, C. Hu, C. Chen, Z. Deng, J. Luo, S. P. Ong, Quantum-accurate spectral neighbor analysis potential models for Ni-Mo binary alloys and fcc metals, *Phys. Rev. B* 98 (2018) 94104.
 - [72] MatWeb, <http://www.matweb.com/>, 2019. Last accessed 14 April 2019.

- [73] M. de Jong, W. Chen, T. Angsten, A. Jain, R. Notestine, A. Gamst, M. Sluiter, C. Krishna Ande, S. van der Zwaag, J. J. Plata, C. Toher, S. Curtarolo, G. Ceder, K. A. Persson, M. Asta, Charting the complete elastic properties of inorganic crystalline compounds, *Scientific Data* 2 (2015) 150009.
- [74] W. T. Read, W. Shockley, V. Number, Dislocation Models of Crystal Grain Boundaries, *Phys. Rev.* 78 (1950) 275–289.

Supplementary Information

Grain Boundary Properties of Elemental Metals

Hui Zheng^{a,1}, Xiang-Guo Li^{a,1}, Richard Tran^a, Chi Chen^a, Matthew Horton^b, Donny Winston^b, Kristin Aslaug Persson^{b,c}, Shyue Ping Ong^{a,*}

^a*Department of NanoEngineering, University of California San Diego, 9500 Gilman Dr, Mail Code 0448, La Jolla, CA 92093-0448, United States*

^b*Environmental Energy Technologies Division, Lawrence Berkeley National Laboratory, Berkeley, CA 94720, United States*

^c*Department of Materials Science & Engineering, University of California Berkeley, Berkeley, CA 94720-1760, United States*

*Corresponding author

Email address: `ongsp@eng.ucsd.edu` (Shyue Ping Ong)

¹These authors contributed equally

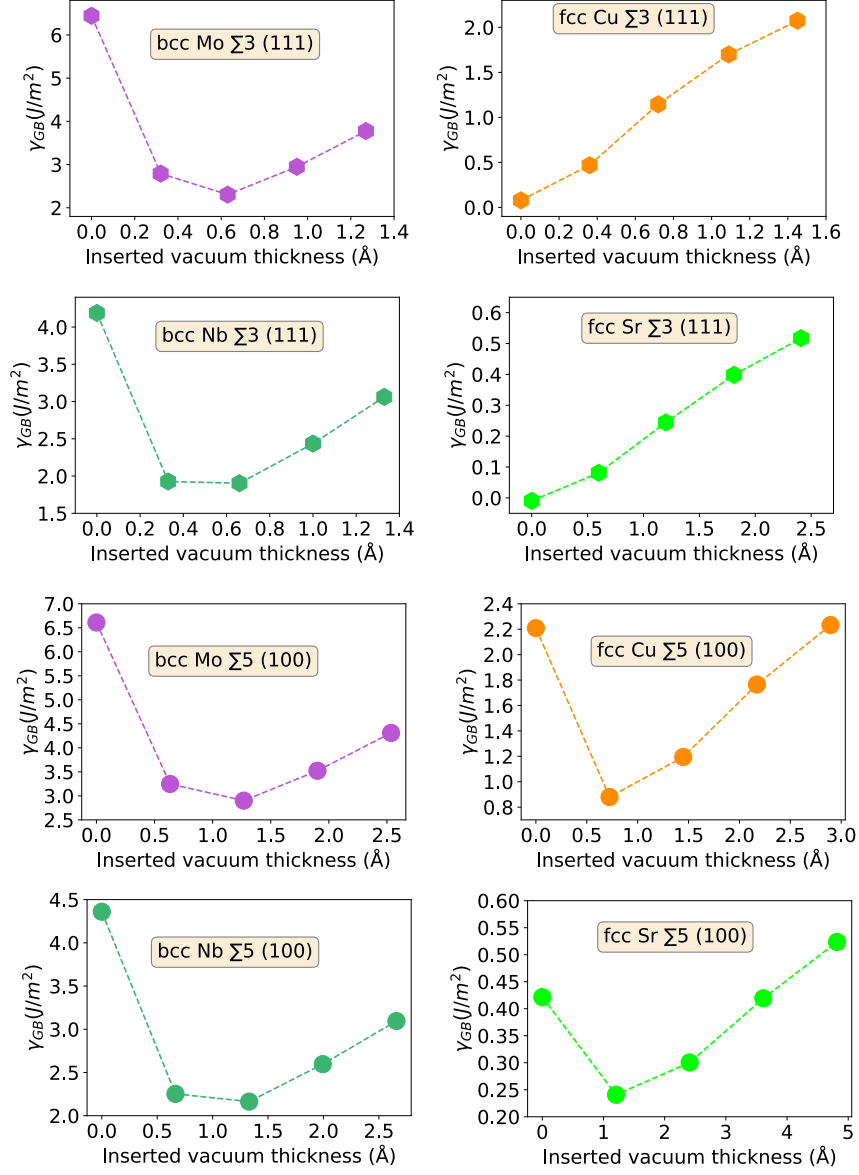


Figure 1: Lattice translation tests (along c direction) for twist GBs.

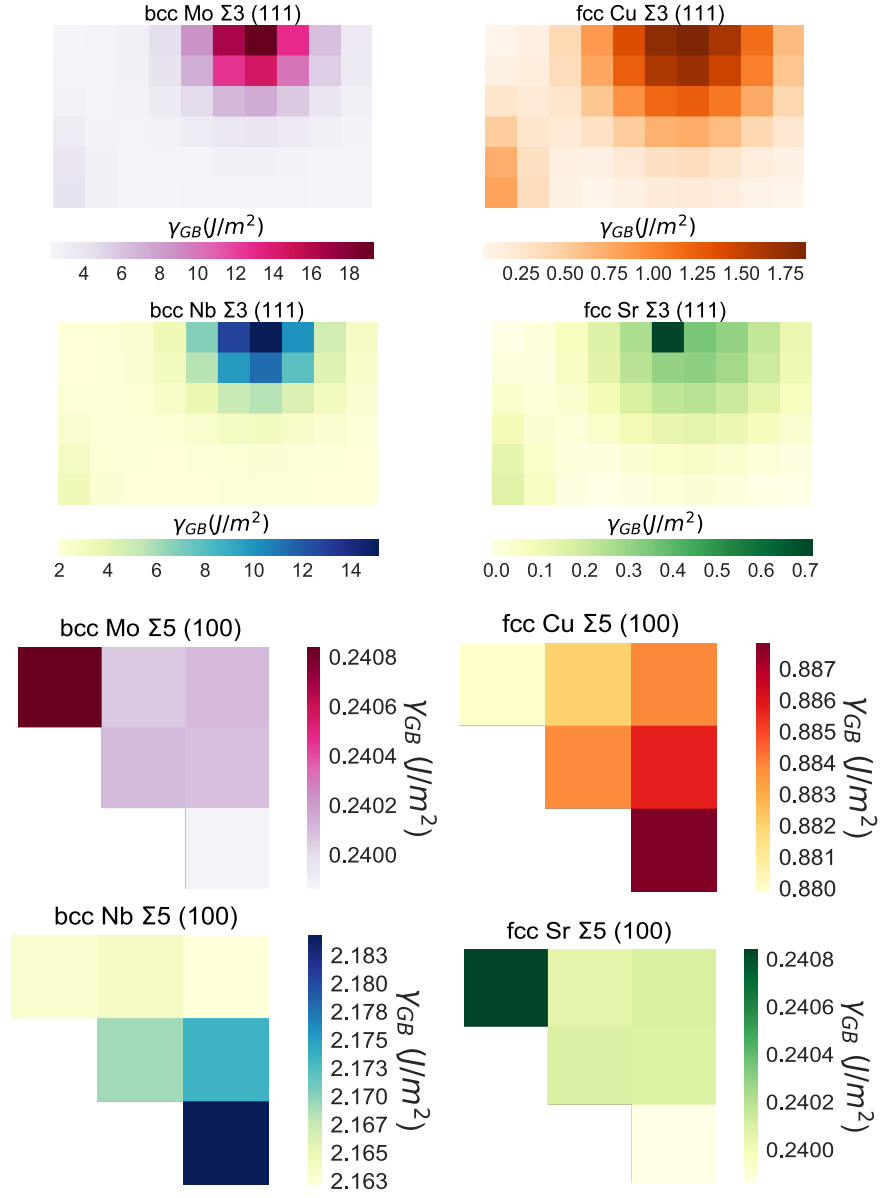


Figure 2: Lattice translation tests (along a and b directions) for twist GBs.

Table 1: Grain boundary energies of cubic elements

sigma	$\Sigma 3$	$\Sigma 3$	$\Sigma 3$	$\Sigma 5$	$\Sigma 5$	$\Sigma 5$	$\Sigma 7$	$\Sigma 7$	$\Sigma 9$	$\Sigma 9$
plane	(011)	(111)	(112)	(001)	(012)	(013)	(111)	(123)	(011)	(122)
Ba	0.045	0.182	0.026	0.279	0.144	0.161	0.210	0.135	0.098	0.187
Cr	0.675	1.981	0.645	2.646	2.195	1.977	2.335	1.901	1.178	2.253
Cs	-0.002	0.013	-0.000	0.021	0.013	0.021	0.025	0.011	-0.004	0.019
Fe	0.508	1.598	0.423	2.243	1.892	1.560	1.904	1.419	0.970	1.754
K	0.032	0.077	0.025	0.088	0.057	0.073	0.058	0.063	0.023	0.071
Li	0.046	0.171	0.054	0.269	0.150	0.156	0.187	0.142	0.082	0.202
Mo	0.503	1.743	0.480	2.432	2.029	1.727	2.210	1.732	1.040	2.064
Na	0.063	0.123	0.044	0.138	0.082	0.132	0.123	0.086	0.074	0.129
Nb	0.294	1.286	0.252	1.492	1.242	1.200	1.343	1.018	0.598	1.271
Rb	0.001	0.048	0.008	0.060	0.034	0.045	0.037	0.026	0.008	0.043
Ta	0.334	1.526	0.289	1.925	1.412	1.438	1.558	1.216	0.732	1.508
V	0.322	1.176	0.258	1.383	1.204	1.262	1.255	0.941	0.611	1.210
W	0.714	2.242	0.665	3.205	2.654	2.204	2.866	2.327	1.400	2.806
Ag	0.545	0.069	0.427	0.419	0.593	0.553	0.208	0.542	0.710	0.507
Al	0.456	-0.004	0.310	0.383	0.532	0.476	0.135	0.501	0.713	0.430
Au	0.458	0.026	0.338	0.323	0.520	0.447	0.175	0.441	0.607	0.393
Ca	0.239	0.018	0.204	0.262	0.303	0.302	0.109	0.307	0.383	0.291
Ce	0.496	0.219	0.489	0.578	0.516	0.580	0.285	0.539	0.622	0.485
Cu	0.848	0.071	0.634	0.751	0.997	0.882	0.370	0.916	1.166	0.856
Ir	1.857	0.352	1.616	1.296	2.186	1.728	0.856	1.866	2.246	1.578

Ni	1.210	-0.007	1.150	1.088	1.383	1.262	0.512	1.327	1.668	1.161
Pb	0.242	0.067	0.221	0.224	0.281	0.243	0.062	0.229	0.313	0.243
Pd	0.886	0.072	0.682	0.718	1.003	0.898	0.319	0.950	1.189	0.852
Pt	0.864	0.176	0.675	0.616	1.094	0.889	0.279	0.885	1.165	0.795
Rh	1.552	0.082	1.250	1.172	1.680	1.447	0.655	1.541	1.854	1.311
Sr	0.187	-0.010	0.159	0.199	0.234	0.237	0.088	0.240	0.310	0.225
Th	0.684	0.175	0.662	0.775	0.758	0.823	0.385	0.817	0.941	0.770
Yb	0.243	0.003	0.198	0.257	0.301	0.302	0.130	0.310	0.397	0.294

Table 2: Grain boundary energies of hcp elements

	Be	Cd	Co	Dy	Er	Gd	Hf	Ho	La
$\Sigma 7(0001)$	1.121	0.116	0.722	0.264	0.318	0.201	0.411	0.297	0.139
	Lu	Mg	Nd	Os	Pm	Pr	Re	Ru	Sc
$\Sigma 7(0001)$	0.342	0.200	0.208	1.578	0.217	0.195	0.970	1.119	0.294
	Sm	Tb	Tc	Ti	Tl	Tm	Y	Zn	Zr
$\Sigma 7(0001)$	0.227	0.242	0.671	0.365	0.074	0.328	0.216	0.141	0.314

Table 3: Work of separation (W_{sep}) of cubic elements

sigma	$\Sigma 3$	$\Sigma 3$	$\Sigma 3$	$\Sigma 5$	$\Sigma 5$	$\Sigma 5$	$\Sigma 7$	$\Sigma 7$	$\Sigma 9$	$\Sigma 9$
plane	(011)	(111)	(112)	(001)	(012)	(013)	(111)	(123)	(011)	(122)
Ag	1.187	1.476	1.309	1.201	1.204	1.229	1.337	1.179	1.023	1.142
Al	1.498	1.595	1.649	1.447	1.498	1.512	1.456	1.427	1.242	1.466
Au	1.197	1.458	1.305	1.399	1.291	1.365	1.309	1.255	1.048	1.167
Ba	0.578	0.592	0.721	0.364	0.535	0.534	0.563	0.582	0.526	0.559
Ca	0.844	0.904	0.887	0.654	0.793	0.765	0.813	0.783	0.701	0.819
Ce	1.763	1.817	1.789	1.687	1.906	1.789	1.751	1.817	1.636	1.737
Cr	5.727	4.890	6.402	4.619	4.884	5.069	4.536	4.994	5.225	4.424
Cs	0.123	0.144	0.140	0.124	0.131	0.120	0.132	0.139	0.124	0.131
Cu	2.274	2.557	2.618	2.184	2.197	2.296	2.259	2.241	1.956	2.100
Fe	4.386	3.862	4.794	2.756	3.241	5.308	3.556	3.846	3.924	3.557
Ir	3.802	4.217	3.802	4.339	3.888	4.310	3.712	3.848	3.413	3.595
K	0.185	0.176	0.228	0.155	0.181	0.162	0.195	0.180	0.193	0.183
Li	0.951	0.916	1.023	0.651	0.861	0.839	0.900	0.927	0.915	0.835
Mo	5.092	4.181	6.318	3.931	4.170	4.448	3.715	4.252	4.555	4.066
Na	0.374	0.378	0.495	0.298	0.376	0.338	0.377	0.389	0.363	0.353
Nb	3.854	3.392	4.439	3.059	3.248	3.366	3.335	3.540	3.550	3.347
Ni	3.362	3.854	3.321	3.329	3.410	3.531	3.335	3.309	2.904	3.185
Pb	0.421	0.439	0.382	0.345	0.426	0.452	0.444	0.411	0.350	0.341
Pd	2.262	2.605	2.545	2.333	2.249	2.370	2.357	2.222	1.959	2.141
Pt	2.878	2.782	2.851	3.067	2.680	2.866	2.678	2.652	2.577	2.404

Rb	0.164	0.161	0.187	0.129	0.149	0.135	0.172	0.164	0.157	0.151
Rh	3.109	3.896	3.370	3.480	3.318	3.541	3.324	3.272	2.807	3.138
Sr	0.628	0.695	0.658	0.494	0.590	0.569	0.597	0.574	0.505	0.543
Ta	4.350	3.875	5.050	3.016	3.643	3.649	3.842	3.986	3.952	3.751
Th	1.953	2.495	-0.000	1.895	1.879	1.814	2.285	1.820	1.729	1.866
V	4.521	4.225	5.131	3.379	3.816	3.678	4.146	4.352	4.232	4.089
W	5.743	4.689	6.123	4.703	4.694	5.219	4.065	4.595	5.057	4.343
Yb	0.778	0.899	0.803	0.608	0.717	0.701	0.772	0.711	0.624	0.675

Table 4: Work of separation (W_{sep}) of hcp elements

	Be	Cd	Co	Dy	Er	Gd	Hf	Ho	La
$\Sigma 7(0001)$	2.460	0.284	3.493	1.714	1.790	1.481	3.007	1.751	1.252
	Lu	Mg	Nd	Os	Pm	Pr	Re	Ru	Sc
$\Sigma 7(0001)$	1.911	0.890	1.430	4.262	1.519	1.373	4.192	4.035	2.240
	Sm	Tb	Tc	Ti	Tl	Tm	Y	Zn	Zr
$\Sigma 7(0001)$	1.557	1.672	3.797	3.566	0.437	1.833	1.793	0.554	2.907

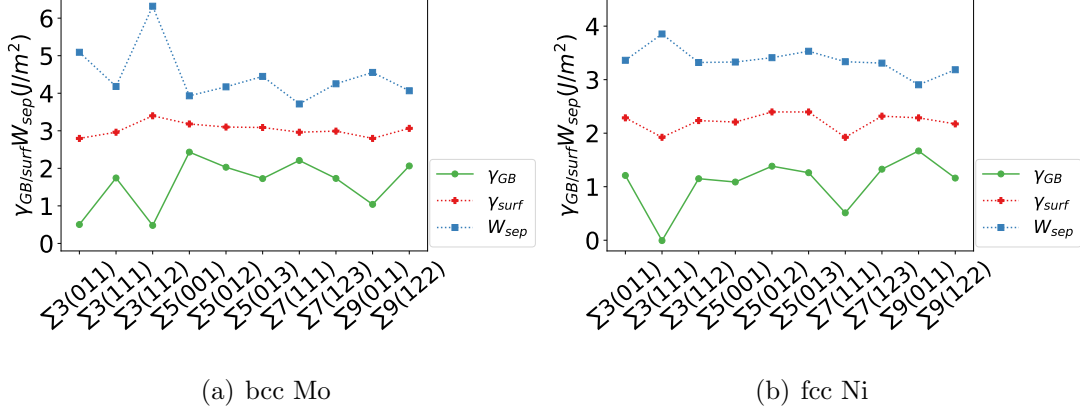


Figure 3: The γ_{surf} varies moderately across different surfaces while the γ_{GB} varies dramatically across different GB types. This causes the near-linear relationship between γ_{GB} and W_{sep} as shown in Figure S4.

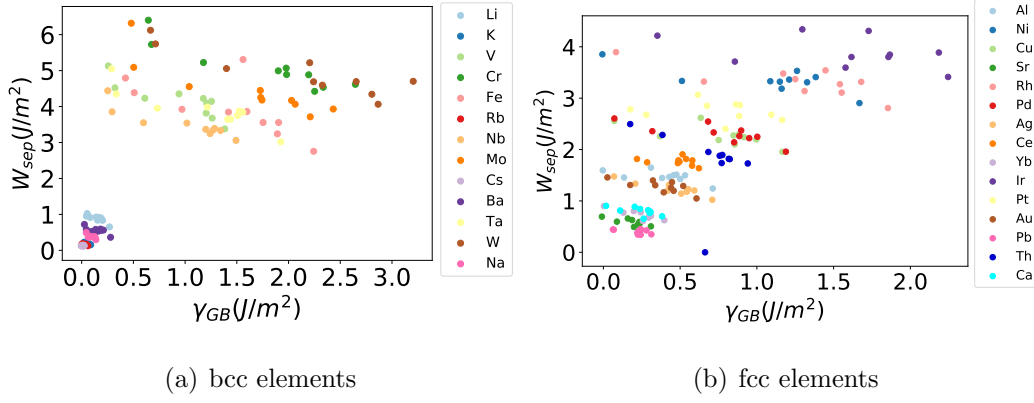


Figure 4: The near linear trend between work of separation and GB energy

Table 5: DFT calculated Grain boundary energies from references

	element	GB type	This work γ_{GB}	Ref γ_{GB}	functional	ref.
0	Mo	$\Sigma 3[1\ 1\ 0]$ (112)	0.480	0.544	PBEsol	[1]
1	Mo	$\Sigma 3[1\ 1\ 0]$ (111)	1.743	1.931	PBEsol	[1]
2	Mo	$\Sigma 5[1\ 0\ 0]$ (013)	1.727	1.813	PBEsol	[1]
3	Mo	$\Sigma 7[1\ 1\ 1]$ (123)	1.732	1.889	PBEsol	[1]
4	Fe	$\Sigma 3[1\ 1\ 0]$ (112)	0.423	0.509	PBEsol	[1]
5	Fe	$\Sigma 3[1\ 1\ 0]$ (111)	1.598	1.785	PBEsol	[1]
6	Fe	$\Sigma 5[1\ 0\ 0]$ (013)	1.560	1.666	PBEsol	[1]
7	Fe	$\Sigma 7[1\ 1\ 1]$ (123)	1.419	1.631	PBEsol	[1]
8	W	$\Sigma 3[1\ 1\ 0]$ (112)	0.665	0.655	PBEsol	[1]
9	W	$\Sigma 3[1\ 1\ 0]$ (111)	2.242	2.440	PBEsol	[1]
10	W	$\Sigma 5[1\ 0\ 0]$ (013)	2.204	2.266	PBEsol	[1]
11	W	$\Sigma 7[1\ 1\ 1]$ (123)	2.327	2.371	PBEsol	[1]
12	Fe	$\Sigma 3[1\ 1\ 0]$ (110)	0.508	0.520	GGA-PBE	[2]
13	Fe	$\Sigma 9[1\ 1\ 0]$ (221)	1.754	1.660	GGA-PBE	[2]
14	Fe	$\Sigma 5[1\ 0\ 0]$ (110)	2.243	2.120	GGA-PBE	[2]
15	Fe	$\Sigma 7[1\ 1\ 1]$ (123)	1.419	1.460	GGA-PBE	[2]
16	Fe	$\Sigma 3[1\ 1\ 0]$ (112)	0.423	0.450	GGA-PBE	[2]
17	Fe	$\Sigma 3[1\ 1\ 0]$ (111)	1.598	1.570	GGA-PBE	[2]
18	Fe	$\Sigma 3[1\ 0\ 0]$ (013)	1.560	1.570	GGA-PBE	[2]
19	Fe	$\Sigma 5[1\ 0\ 0]$ (012)	1.892	1.640	GGA-PBE	[2]
20	Fe	$\Sigma 3[1\ 1\ 0]$ (111)	1.598	1.610	GGA-PBE	[3]

	element	GB type	This work γ_{GB}	Ref γ_{GB}	functional	ref.
21	Fe	$\Sigma 3[1\ 1\ 0]$ (111)	1.598	1.570	GGA-PW91	[4]
22	Fe	$\Sigma 3[1\ 1\ 0]$ (111)	1.598	1.520	GGA	[5]
23	Fe	$\Sigma 3[1\ 1\ 0]$ (112)	0.423	0.340	GGA	[5]
24	Fe	$\Sigma 3[1\ 1\ 0]$ (112)	0.423	0.470	GGA-PW91	[6]
25	Fe	$\Sigma 5[1\ 0\ 0]$ (013)	1.560	1.530	GGA-PW91	[6]
26	Fe	$\Sigma 5[1\ 0\ 0]$ (013)	1.560	1.630	GGA-PBE	[7]
27	Fe	$\Sigma 5[1\ 0\ 0]$ (013)	1.560	1.489	GGA	[5]
28	Fe	$\Sigma 5[1\ 0\ 0]$ (012)	1.892	2.000	GGA-PW91	[4]
29	Ta	$\Sigma 5[1\ 0\ 0]$ (013)	1.438	1.544	LDFT	[8]
30	W	$\Sigma 5[1\ 0\ 0]$ (013)	2.204	2.235	LDFT	[8]
31	Mo	$\Sigma 5[1\ 0\ 0]$ (013)	1.727	1.700	LDFT	[8]
32	Nb	$\Sigma 5[1\ 0\ 0]$ (013)	1.200	1.288	LDFT	[8]
33	Cu	$\Sigma 5[1\ 0\ 0]$ (012)	0.997	0.920	GGA-PBE	[9]
34	Cu	$\Sigma 3[1\ 1\ 0]$ (111)	0.071	0.020	GGA-PBE	[9]
35	Cu	$\Sigma 3[1\ 1\ 0]$ (112)	0.634	0.570	GGA-PBE	[9]
36	Ni	$\Sigma 5[1\ 0\ 0]$ (012)	1.383	1.230	GGA-PBE	[9]
37	Ni	$\Sigma 3[1\ 1\ 0]$ (111)	-0.007	0.040	GGA-PBE	[9]
38	Ni	$\Sigma 3[1\ 1\ 0]$ (111)	1.150	0.840	GGA-PBE	[9]
39	Al	$\Sigma 3[1\ 1\ 0]$ (112)	0.310	0.426	LDA	[10]

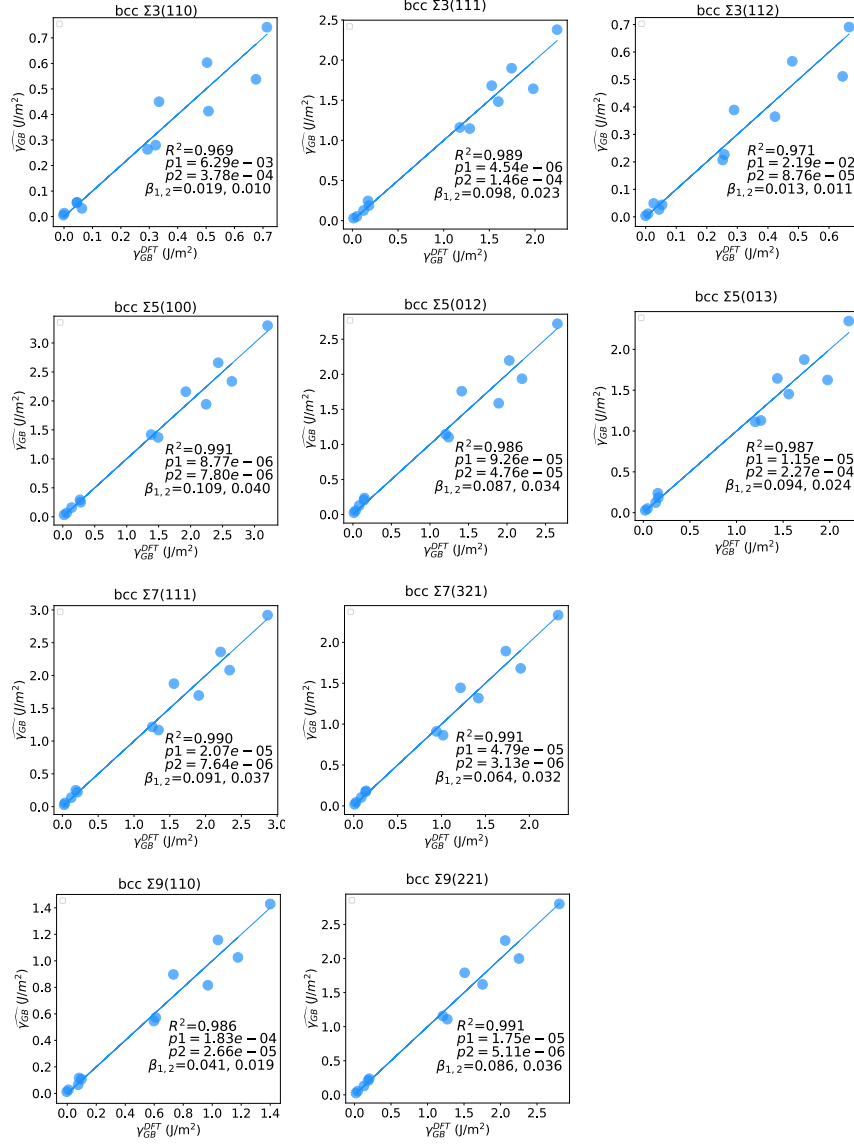


Figure 5: Fitting models for all the GB types of bcc elements with $\gamma_{GB} = \beta_1 E_{coh} a_0^{-2} + \beta_2 G \cdot a_0$.

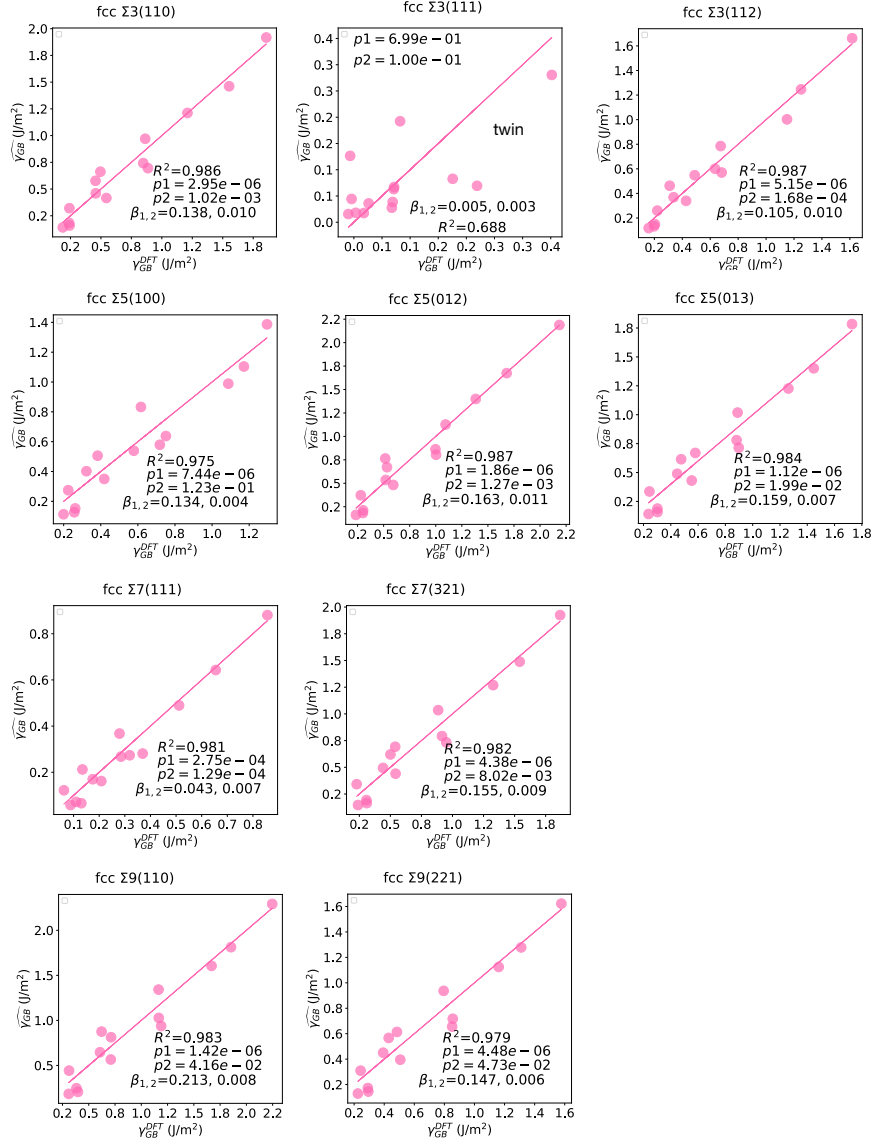


Figure 6: Fitting models for all the GB types of fcc elements with $\gamma_{GB} = \beta_1 E_{coh} a_0^{-2} + \beta_2 G \cdot a_0$.

References

References

- [1] D. Scheiber, R. Pippan, P. Puschnig, L. Romaner, Ab initio calculations of grain boundaries in bcc metals, *Modelling and Simulation in Materials Science and Engineering* 24 (2016) 035013.
- [2] J. Wang, G. K. H. Madsen, R. Drautz, Grain boundaries in bcc-fe: a density-functional theory and tight-binding study, *Modelling and Simulation in Materials Science and Engineering* 26 (2018) 025008.
- [3] S. K. Bhattacharya, S. Tanaka, Y. Shiihara, M. Kohyama, Ab initio study of symmetrical tilt grain boundaries in bcc fe: structural units, magnetic moments, interfacial bonding, local energy and local stress, *Journal of Physics: Condensed Matter* 25 (2013) 135004.
- [4] E. Wachowicz, T. Ossowski, A. Kiejna, Cohesive and magnetic properties of grain boundaries in bcc Fe with Cr additions, *Phys. Rev. B* 81 (2010) 94104.
- [5] N. Gao, C. C. Fu, M. Samaras, R. Schäublin, M. Victoria, W. Hoffelner, Multiscale modelling of bi-crystal grain boundaries in bcc iron, *Journal of Nuclear Materials* 385 (2009) 262–267.
- [6] Y. A. Du, L. Ismer, R. Jutta, T. Hickel, J. Neugebauer, R. Drautz, First-principles study on the interaction of H interstitials with grain boundaries in α and γ -Fe, *Phys. Rev. B* 84 (2011) 144121.

- [7] M. Čák, M. Šob, J. Hafner, First-principles study of magnetism at grain boundaries in iron and nickel, *Physical Review B - Condensed Matter and Materials Physics* 78 (2008) 1–10.
- [8] T. Ochs, C. Elsässer, M. Mrovec, V. Vitek, J. Belak, J. A. Moriarty, Symmetrical tilt grain boundaries in bcc transition metals: Comparison of semiempirical with ab-initio total-energy calculations, *Philosophical Magazine A: Physics of Condensed Matter, Structure, Defects and Mechanical Properties* 80 (2000) 2405–2423.
- [9] J. J. Bean, K. P. McKenna, Origin of differences in the excess volume of copper and nickel grain boundaries, *Acta Materialia* 110 (2016) 246–257.
- [10] A. F. Wright, S. R. Atlas, Density-functional calculations for grain boundaries in aluminum, *Phys. Rev. B* 50 (1994) 15248–15260.